Hydrodynamic effects on spinodal decomposition kinetics in planar lipid bilayer membranes

Jun Fan,[1] Tao Han,[1] and Mikko Haataja[2,a)]
[1]*Department of Mechanical and Aerospace Engineering, Princeton University, Princeton, New Jersey 08544, USA*
[2]*Department of Mechanical and Aerospace Engineering, Princeton Institute for the Science and Technology of Materials (PRISM), and Program in Applied and Computational Mathematics (PACM), Princeton University, Princeton, New Jersey 08544, USA*

(Received 11 August 2010; accepted 1 November 2010; published online 15 December 2010)

The formation and dynamics of spatially extended compositional domains in multicomponent lipid membranes lie at the heart of many important biological and biophysical phenomena. While the thermodynamic basis for domain formation has been explored extensively in the past, domain growth in the presence of hydrodynamic interactions both within the (effectively) two-dimensional membrane and in the three-dimensional solvent in which the membrane is immersed has received little attention. In this work, we explore the role of hydrodynamic effects on spinodal decomposition kinetics via continuum simulations of a convective Cahn–Hilliard equation for membrane composition coupled to the Stokes equation. Our approach explicitly includes hydrodynamics both within the planar membrane and in the three-dimensional solvent in the viscously dominated flow regime. Numerical simulations reveal that dynamical scaling breaks down for critical lipid mixtures due to distinct coarsening mechanisms for elongated versus more isotropic compositional lipid domains. The breakdown in scaling should be readily observable in experiments on model membrane systems. © *2010 American Institute of Physics*. [doi:10.1063/1.3518458]

I. INTRODUCTION

Lipid bilayer membranes are ubiquitous in mammalian cells and facilitate the interaction between a cell and its surroundings. Furthermore, lipid membranes are employed in important biomedical applications, such as vehicles for targeted drug delivery. Notably, membrane "microstructure" (that is, local lipid and protein compositions, etc.) directly controls the mechanical, physical, and biochemical properties of the system.

At the mesoscale, lipid bilayer membranes can be regarded as effectively two-dimensional (2D) systems embedded within a three-dimensional (3D) aqueous solvent. The membrane may be compositionally homogeneous or heterogeneous, and structurally either solidlike (gel) or liquid, or display coexistence between gel and liquid phases or multiple liquid phases. Indeed, several studies employing model membrane systems have provided a plethora of important insight into both the structure and dynamics of compositional lipid domains in lipid vesicles.[1–5]

While the thermodynamic basis for compositional lipid microdomain formation in synthetic membranes has been explored extensively in the past, the roles of membrane and exterior fluid hydrodynamics on domain formation kinetics have received relatively little attention, despite the fact that these hydrodynamic interactions can strongly influence the kinetics. A case in point is the asymptotic dynamic behavior of a lipid membrane system in the vicinity of a critical point (CP). Conventional wisdom predicts that hydrodynamics can be neglected asymptotically close to the CP. In contrast, Haataja has developed a theory, which predicts a novel scaling behavior for lipid transport coefficients near the CP due to hydrodynamic interactions for membranes immersed in a bulk solvent.[6] This result has important ramifications for the dynamics of compositional domains in both *in vivo* and *in vitro* membranes.

Once an immiscible fluid mixture is quenched below the critical point, on the other hand, phase separation ensues. During the phase separation process, compositional domains emerge and grow with time t; that is, the system coarsens. Importantly, it is often found that a single time-dependent length scale $R(t)$ (such as the average domain size, first zero crossing of the two-point correlation function, etc.) fully characterizes the statistical properties of the coarsening system. More specifically, if all lengths in the system are scaled by $R(t)$, the configurations recorded at different times are asymptotically indistinguishable in a statistical sense. This is called dynamical scaling, and in the scaling regime $R(t)$ usually obeys $R \sim t^{\beta}$ with β denoting the so-called growth exponent. Moreover, in such scale-invariant systems, all characteristic lengths will scale with the same exponent β. Finally, at the critical composition, the two emerging phases have equal area (volume) fractions in 2D (3D) and often form interconnected morphologies, while off-critical compositions outside the spinodal region usually lead to a droplet morphology at late times. For a comprehensive review on coarsening phenomena, see Ref. 7.

Now, experiments probing phase separation dynamics in lipid membranes have painted a rather confusing picture. Saeki *et al.*[8] investigated the domain growth kinetics in a

a)Electronic mail: mhaataja@princeton.edu

cell-sized liposome, and found that the average domain size R increases with time t as $R \sim t^{0.15}$ for off-critical mixtures. Yanagisawa *et al.*[9] in turn studied the growth dynamics of domains on ternary fluid vesicles. They found two types of coarsening processes, namely, "normal" and "trapped" coarsening. In the former case, $R \sim t^{2/3}$, while in the latter, the domain coarsening is suppressed beyond a critical domain size. Interestingly, $R \sim t^{2/3}$ scaling was reported for both critical and off-critical lipid mixtures. Notably, the experimental observations from Refs. 8 and 9 do not agree as far as the coarsening kinetics are concerned.

On the other hand, computational studies of domain formation dynamics in lipid membranes in contact with a solvent do not agree on the coarsening kinetics either. Laradji and Kumar[10,11] investigated the dynamics of domain growth in fluid vesicles at an off-critical composition using dissipative particle dynamics (DPD) simulations. For spherical vesicles with identical compositions for the two monolayers, $R \sim t^{0.3}$,[10] while for spherical vesicles with asymmetric composition between the two monolayers the domain growth was slower with $R \sim t^{0.13}$ followed by $R \sim t^{0.3}$ at late times.[11] Ramachandran *et al.*[12] in turn simulated spinodal decomposition in both curved and planar membranes at the critical composition also using DPD simulations. For both cases, $R \sim t^{1/2}$. More recently, Ramachandran *et al.*[13] simulated spinodal decomposition in a thin liquid film using DPD, both in the presence and absence of a solvent. In the former case, they found that $R \sim t^{1/3}$, while in the latter case $R \sim t^{1/2}$, highlighting the importance of the solvent on coarsening kinetics. Interestingly, a very recent continuum study also obtained $R \sim t^{1/2}$ for spinodal decomposition (SD) dynamics in planar membranes coupled to a bulk solvent.[14] In all, both experimental and computational studies have painted a rather confusing picture of the role of hydrodynamics on coarsening kinetics in lipid membranes.

The goal of this paper is to clarify the effects of membrane and solvent hydrodynamics on SD kinetics in planar lipid bilayer membranes for critical lipid compositions. More specifically, by employing a continuum approach, we demonstrate that dynamical scaling is absent in SD kinetics in lipid bilayer membranes due to the presence of hydrodynamic interactions. While such scaling violations have been observed previously in strictly two-dimensional simulations of phase-separating binary fluids,[15–17] we have generalized these 2D simulation results to fully 3D viscously dominated flows, including both SD kinetics within the membrane and solvent-mediated interactions. The breakdown in scaling should be readily observable in experiments on model membrane systems.

The rest of this paper is organized as follows. In Sec. II we first introduce the continuum approach employed in this work, while Sec. III contains both a discussion of the numerical scheme adopted in the simulations and a presentation of simulation results. Finally, a discussion and concluding remarks can be found in Sec. IV.

II. THEORETICAL APPROACH

For simplicity, we assume that the membrane comprises of two lipid types, A and B, with local concentrations c_A and c_B, respectively. Now, within the membrane, the order parameter (OP) corresponding to the dimensionless concentration field is defined via $\psi \equiv (c_A(\mathbf{r},t) - c_B(\mathbf{r},t))/2\bar{c}$, where $\bar{c}$ denotes the critical composition. The OP evolves according to the convective Cahn–Hilliard equation[14,18]

$$\frac{\partial \psi}{\partial t} + \nabla \cdot (\psi \mathbf{u}) = \lambda_0 \nabla^2 \mu_\psi, \tag{1}$$

where λ_0 denotes the compositional mobility, $\mu_\psi \equiv \delta F/\delta\psi$ denotes the chemical potential with a phenomenological free-energy given by[18]

$$F = \int d\mathbf{r} \left[\frac{1}{2}(\nabla\psi)^2 - \frac{\psi^2}{2} + \frac{\psi^4}{4} \right], \tag{2}$$

and $\mathbf{u}(\mathbf{r},t)$ denotes the local velocity field within the membrane. Note that this choice of F implies that the interface width (or, equivalently, the mean-field correlation length ξ) has unit thickness; that is, all lengths are measured in units of ξ. In principle, a stochastic noise term can be added to Eq. (1) to account for the presence of thermal fluctuations. In this work, we have ignored it, but will revisit the issue in Sec. IV. We have also assumed that the bilayer is symmetric with respect to lipid compositions and that the compositions are coupled in the two leaflets such that they become spatially synchronized, as has been observed in experiments.[2] Furthermore, to clearly identify the role of hydrodynamic effects on coarsening, we have ignored couplings between the local composition and membrane curvature, and assume that the membrane remains perfectly planar.

Turning now to membrane and solvent hydrodynamics, we first estimate that the Reynolds number Re characterizing the flow fields within the membrane and solvent is given by $Re = uR/\nu \sim 10^{-5}$ based on experimental data from Refs. 8 and 9. Here, $u \sim 10^{-6}$ m/s, $R \sim 10^{-5}$ m and $\nu \sim 10^{-6}$ m^2/s denote the characteristic velocity, domain size, and kinematic viscosity of the solvent, respectively. The membrane flow field $\mathbf{u}(\mathbf{r},t)$ is thus dominated by viscosity in this regime and satisfies the Stokes equation,

$$\eta_M \nabla^2 \mathbf{u} - \nabla p + \mathbf{W} - \mathbf{F} = 0, \tag{3}$$

with the incompressibility condition

$$\nabla \cdot \mathbf{u} = 0, \tag{4}$$

where η_M denotes the (dynamic) lipid membrane viscosity, assumed constant in this work. Here, $\mathbf{W}(\mathbf{r},t) = -\psi\nabla\mu_\psi$ accounts for the impact of compositional variations in the membrane stress tensor, while the effective membrane pressure p is employed to enforce the incompressibility condition. In the limit where compositional interfaces are sharp, $\mathbf{W}$ incorporates line tension forces acting normal to the interfaces, and which locally drive fluid flow within the membrane. Finally, the effective force $\mathbf{F}$ in Eq. (3) arises from the coupling between the membrane and the solvent flow fields via the no-slip boundary condition.[19]

Now, it can be shown that velocity field is given in Fourier representation by

$$\hat{\mathbf{u}}(\mathbf{q},t) = \hat{\overleftrightarrow{T}} \cdot \hat{\mathbf{W}}, \tag{5}$$

where $\hat{\mathbf{W}}$ denotes the Fourier transform of the membrane compositional force $\mathbf{W}$, and where the components of the modified Oseen tensor $\hat{\hat{T}}$ are given by[20]

$$\hat{T}_{\alpha\beta}(\mathbf{q}) = \frac{1}{\eta_M q^2 + 2\eta_S q}\left(\delta_{\alpha\beta} - \frac{q_\alpha q_\beta}{q^2}\right) = \frac{1}{q\eta_S(q\ell_H + 2)}\left(\delta_{\alpha\beta} - \frac{q_\alpha q_\beta}{q^2}\right). \quad (6)$$

Furthermore, $q = \left(q_x^2 + q_y^2\right)^{1/2}$, η_S denotes the viscosity of the solvent, and $\ell_H \equiv \eta_M/\eta_S$ denotes the so-called hydrodynamic length.[21] The significance of ℓ_H is that the membrane hydrodynamics is effectively 2D (3D) on spatial scales smaller than (greater than) ℓ_H. In the quantitative part of this study, we will focus on three cases with regard to ℓ_H: $\ell_H \to \infty$, $\ell_H \to 0$, and finite ℓ_H. These choices correspond to cases where the hydrodynamic effects are confined within the membrane alone, dominated by the solvent, or shared between both the membrane and the solvent, respectively. It should be noted that the $\ell_H = \infty$ case, which corresponds to a strictly 2D system decoupled from the solvent, has been theoretically studied extensively in the past.[16,17,22–31] Finally, in the simulations detailed below, we systematically vary the magnitudes of the viscosities in order to explore the role of the (nominal) Peclét number $Pe \sim \min[\xi^2\eta_M^{-1}\lambda_0^{-1}, \xi\eta_S^{-1}\lambda_0^{-1}]$ in the coarsening kinetics. In particular, $Pe \gg 1$ implies that the advective term dominates over the nonlinear diffusion one in Eq. (1), while for $Pe \ll 1$ the opposite is true.

III. NUMERICAL SIMULATIONS

Before turning to the description of the results from numerical simulations, we first present the numerical scheme we have employed. The numerical scheme is then applied to elucidate SD kinetics of lipid bilayer membranes at the critical composition in the presence of hydrodynamics.

A. Numerical scheme

A splitting scheme (Trotter's formula)[32] was adopted to update the order parameter field ψ via two steps. In the first step, the order parameter is updated by considering only the effect of the convective term,

$$\psi_{i,j}^* = \psi_{i,j} - \Delta t\left[\frac{(\psi u_x)_{i+1,j} - (\psi u_x)_{i-1,j}}{2\Delta x} + \frac{(\psi u_y)_{i,j+1} - (\psi u_y)_{i,j-1}}{2\Delta y}\right], \quad (7)$$

where $\mathbf{u} = [u_x, u_y]$ was obtained by the inverse Fourier transformation of $\hat{\mathbf{u}}$:

$$\hat{u}_x(\mathbf{q}) = \frac{q_y^2\hat{W}_x - q_x q_y \hat{W}_y}{\eta_M q^4 + 2\eta_S q^3}, \quad (8)$$

$$\hat{u}_y(\mathbf{q}) = \frac{q_x^2\hat{W}_y - q_x q_y \hat{W}_x}{\eta_M q^4 + 2\eta_S q^3}. \quad (9)$$

Here, $\hat{\mathbf{W}}$ is the Fourier transform of the discretized $\mathbf{W} = [W_x, W_y]$:

$$W_x = -\psi_{i,j}\frac{\mu_{i+1,j} - \mu_{i-1,j}}{2\Delta x}, \quad (10)$$

$$W_y = -\psi_{i,j}\frac{\mu_{i,j+1} - \mu_{i,j-1}}{2\Delta y}, \quad (11)$$

$$\mu_{i,j} = -\psi_{i,j} + \psi_{i,j}^3 - [\psi_{i+1,j} + \psi_{i-1,j} + \psi_{i,j+1} + \psi_{i,j-1} - 4\psi_{i,j}]/(\Delta x)^2. \quad (12)$$

Next, $\psi_{i,j}^*$ is updated in time based on the nonlinear diffusion part using the standard forward Euler scheme to complete one full numerical integration step,

$$\psi_{i,j} = \psi_{i,j}^* + \Delta t\lambda_0(\mu_{i+1,j}^* + \mu_{i-1,j}^* + \mu_{i,j+1}^* + \mu_{i,j-1}^* - 4\mu_{i,j}^*)/(\Delta x)^2, \quad (13)$$

where $\mu_{i,j}^*$ is obtained from Eq. (12) by replacing $\psi_{i,j}$ with $\psi_{i,j}^*$. The computational domain is $L \times L$ with periodic boundary conditions and box size $L = 1024$. The initial composition was chosen to be homogeneous with small random fluctuations drawn from a Gaussian distribution. In this work, $\lambda_0 = 1$, and the dimensionless grid spacing $\Delta x = \Delta y = 1$ and time step $\Delta t = 0.005$ were employed.

To verify the accuracy of the numerical scheme, we have numerically extracted the relaxation times τ_q of small amplitude, sinusoidal capillary wave fluctuations with wave number q around a planar compositional interface. In this case, it can be shown that[33] in the absence of inertia

$$\tau_q = \frac{4\eta_M}{\sigma q} \quad \text{for } l_H \to \infty$$
$$\tau_q = \frac{2\pi\eta_S}{\sigma q^2} \quad \text{for } l_H \to 0, \quad (14)$$

where σ denotes the surface tension; for the free energy in Eq. (2), $\sigma = 2\sqrt{2}/3$. Numerically extracted τ_q versus q are displayed in Fig. 1 for $\ell_H = 0$ and ∞. It can be seen that the

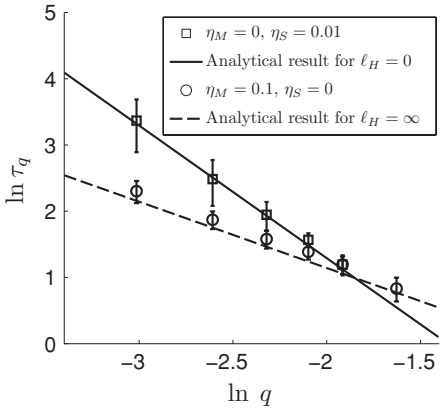

FIG. 1. Relaxation time τ_q of sinusoidal interface perturbation vs q extracted from simulations. Squares and circles correspond to $\ell_H = 0$ and $\ell_H = \infty$, respectively, while solid and dashed lines correspond to the analytical predictions from Eqs. (14). Note that the simulation results are in very good agreement with analytical predictions.

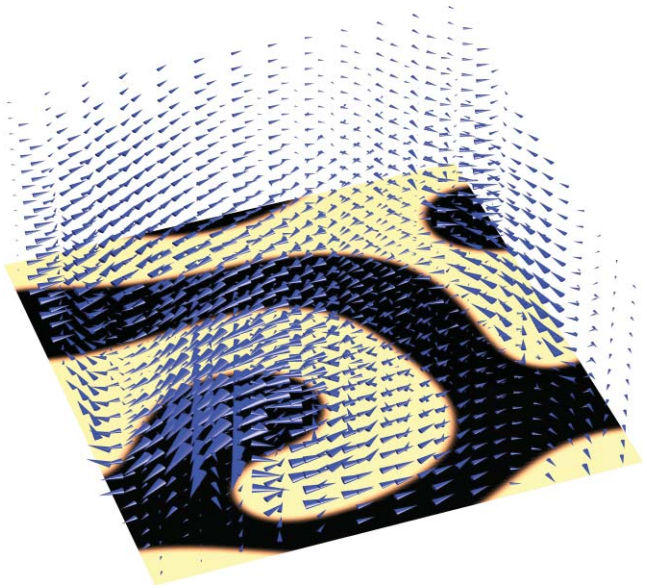

FIG. 2. Representative membrane concentration map and instantaneous solvent flow field. Dark and light colors represent the $\psi = 1$ and $\psi = -1$ phases, respectively. The size and orientation of the cones reflect the magnitude and direction of the 3D solvent velocity field, respectively.

analytical predictions are in very good agreement with simulation results.

Finally, the simulation geometry is shown in Fig. 2, which displays a representative membrane concentration map during SD and the associated 3D solvent flow field. In subsequent figures displaying concentration maps, membrane and solvent flow fields are omitted for clarity.

B. Spinodal decomposition with hydrodynamics. I. Qualitative analysis

Let us now turn to a qualitative discussion of hydrodynamic flow effects on spinodal decomposition kinetics in lipid membranes. More specifically, in this section we will focus on two regimes, namely $\ell_H > 0$ and $\ell_H = 0$. Both cases represent a 2D membrane coupled to 3D solvent flow fields. In the first case, both membrane and solvent flow fields contribute to viscous dissipation, while in the second case, viscous dissipation is completely dominated by the surrounding solvent.

We begin by examining the role of finite hydrodynamic length. More specifically, we have set $\ell_H = 10$ by choosing representative parameters values $(\eta_M, \eta_S) = (1, 0.1)$ and $(0.1, 0.01)$, corresponding to $Pe \sim 1$ and 10, respectively. Resulting concentration maps are shown in Fig. 3. Initially, regardless of the magnitude of η_M, emerging domains are elongated and bi-continuous, and become more isotropic as the line tension-driven coarsening proceeds. Interestingly, at low viscosities corresponding to $Pe \gtrsim 10$, there is an apparent decoupling between the coarsening dynamics of elongated and circular domains. For example, a comparison between panels (e) and (f) in Fig. 3 reveals dramatic changes in both morphologies and sizes of some of the elongated domains, while more isotropic ones embedded within these domains have only been advected by the local flow fields with little change in shape or size. Similar results were obtained for $Pe \gtrsim 10$ in the case where hydrodynamic effects are completely dominated by the surrounding solvent; that is, $\ell_H = 0$. Representative parameter values were set to $(\eta_M, \eta_S) = (0, 0.1)$ and $(0, 0.01)$, corresponding to $Pe \sim 10$ and 100, respectively. The corresponding concentration maps are displayed in Fig 4. Again, a comparison between panels (e) and (f) in

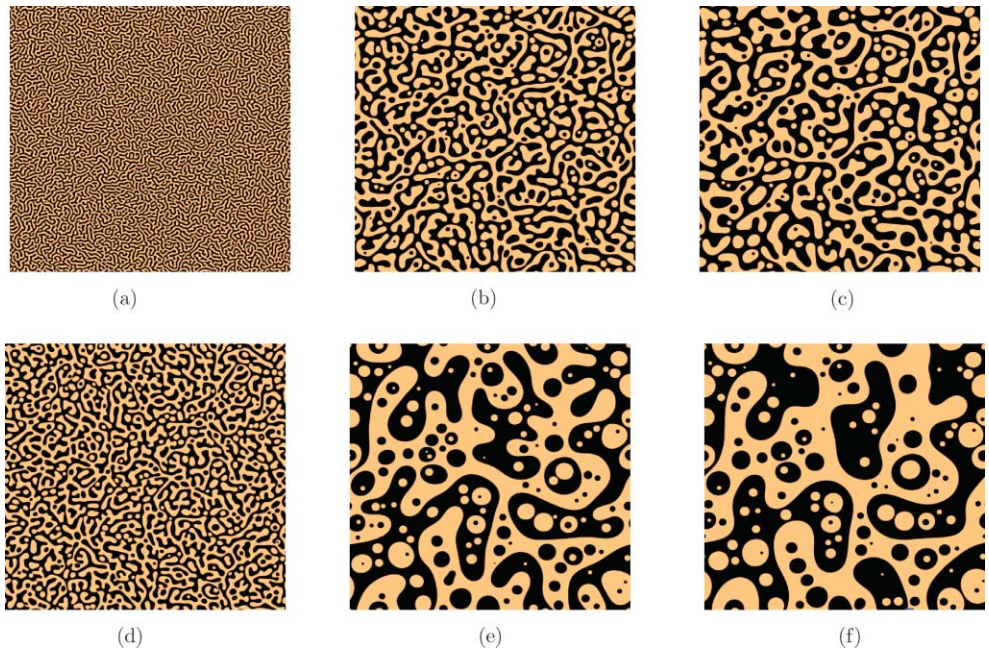

FIG. 3. Concentration maps during spinodal decomposition with $\ell_H = 10$. (a)–(c) $(\eta_M, \eta_S) = (1, 0.1)$. (d)–(f) $(\eta_M, \eta_S) = (0.1, 0.01)$. Time increases from left to right with $t = 55$, 405, and 700. Note the increase in the overall coarsening kinetics as the viscosities are decreased. Also, a comparison between panels (e) and (f) reveals dramatic changes in the morphologies and sizes of some of the elongated domains, while more isotropic ones have changed very little in shape or size. This implies that dynamical scaling breaks down.

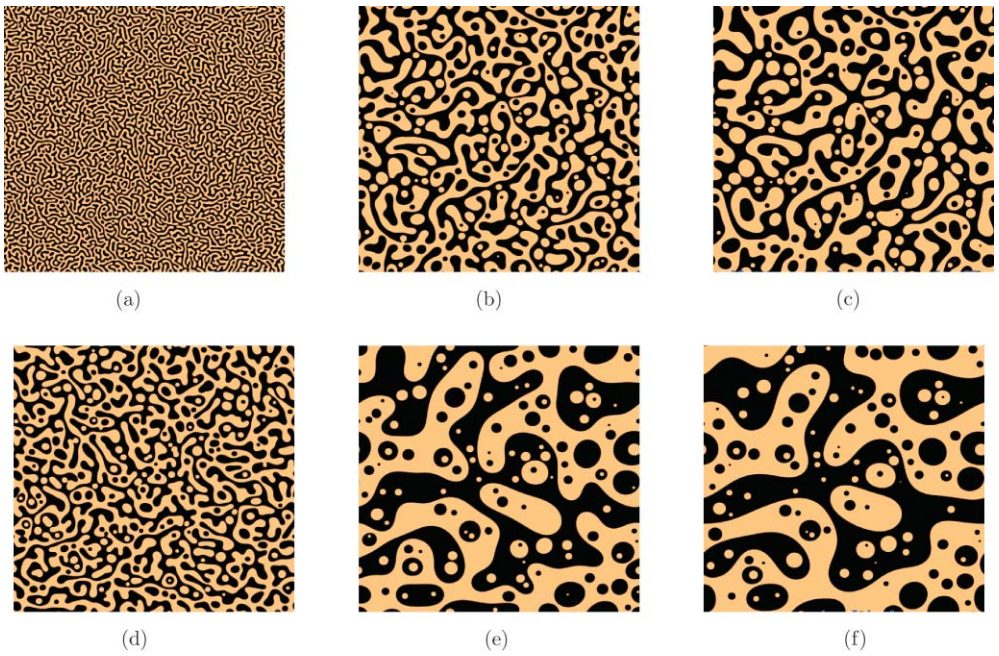

FIG. 4. Concentration maps during spinodal decomposition with $\ell_H = 0$. (a)–(c) $(\eta_M, \eta_S) = (0, 0.1)$. (d)–(f) $(\eta_M, \eta_S) = (0, 0.01)$. Time increases from left to right with $t = 55$, 405, and 700. Again, note the increase in the coarsening rate as the viscosities are decreased. Also, again note the breakdown of dynamical scaling at low viscosities, as more elongated domains undergo rapid morphology and size changes, while more isotropic ones change very little in shape or size.

Fig. 4 reveals dramatic changes in the morphologies and sizes of some of the elongated domains, while more isotropic ones have changed very little in shape or size.

These observations suggest that a single length scale cannot adequately represent the statistical properties of the concentration maps for different times; in other words, dynamical scaling breaks down. Such a breakdown in dynamical scaling has been previously observed in purely 2D phase-separating fluid systems,[15–17] and it is interesting that scaling is not recovered even when 3D solvent flow fields are included. As will be discussed in more detail below, the significance of this result is that different quantitative measures of the domain morphology employed to characterize the coarsening kinetics in the same system will yield widely varying, effective coarsening rates. Curiously, breakdown of dynamical scaling has not been reported in DPD studies of phase-separating lipid membranes[12] or thin liquid films.[13]

For even smaller viscosities (data not shown), we have observed small circular domains nucleate and grow within other droplets. This phenomena is called secondary phase separation due to the so-called interface quench effect.[15] In this case, domains form rapidly due to hydrodynamic flow effects, but the process takes place too quickly for the order parameter to equilibrate; thus, a secondary phase separation commences.[16,17,31]

C. Spinodal decomposition with hydrodynamics. II. Quantitative analysis

Next, in order to quantify the breakdown of dynamical scaling, we have computed the temporal evolution of the average domain size and the (effective) growth exponent. The average domain size R in this study is defined by $R(t) = A_d/\ell_d(t)$, where A_d is the total area of the $\psi = 1$ phase ($A_d = L^2/2$ at the critical composition), and $\ell_d(t)$ is the time-dependent, total interface length between the compositional domains. The data for $R(t)$ are shown in Figs. 5(a)–5(c). We define an effective growth exponent β_{eff} in turn via $\beta_{\text{eff}}(t) = \ln[R(t + \Delta t)/R(t)]/\ln[(t + \Delta t)/t]$, and the corresponding data is shown in Figs. 5(d)–5(f).

The data in Figs. 5(a)–5(c) quantitatively confirm our observations that domain coarsening proceeds faster as the viscosity decreases. With regard to the effective coarsening exponent $\beta_{\text{eff}}(t)$, inspection of Figs. 5(d)–5(f) reveals that low viscosities corresponding to $Pe \gtrsim 10$ are associated with large initial β_{eff} values, with a rapid decrease at later times regardless of the magnitude of ℓ_H. The reason for this is the rapid coarsening of elongated domains, as will be discussed in more detail below. For intermediate viscosity values corresponding to $Pe \sim 1$ and $\ell_H = \infty$, we observe a rather slow decrease from $\beta_{\text{eff}} \approx 0.7$ to 0.3 as the coarsening proceeds. These results are consistent with previous simulations of spinodal decomposition in 2D binary fluids using both Langevin equation[15,17] and lattice Boltzmann[16] approaches.

On the other hand, at intermediate viscosity values corresponding to $Pe \sim 1$ for $\ell_H = 10$, we observe an *apparent* scaling regime with $\beta_{\text{eff}} \approx 0.5$, as shown in Fig. 5(e). Interestingly, a similar scaling exponent was also reported in Ref. 12 based on DPD simulations. However, a closer examination of the data reveals a very slow decrease in β_{eff}, from $\beta_{\text{eff}} \approx 0.5$ at early times to $\beta_{\text{eff}} \approx 0.45$ at the end of the simulation. In other words, this is not a true scaling regime. This observation is in rather stark contrast with very recent simulations of a related continuum model by Camley and Brown,[14] whoclaimed that scaling is observed at finite ℓ_H values with $\beta_{\text{eff}} = 0.5$. In the case of $\ell_H = 0$, no apparent scaling regimes are discernible,

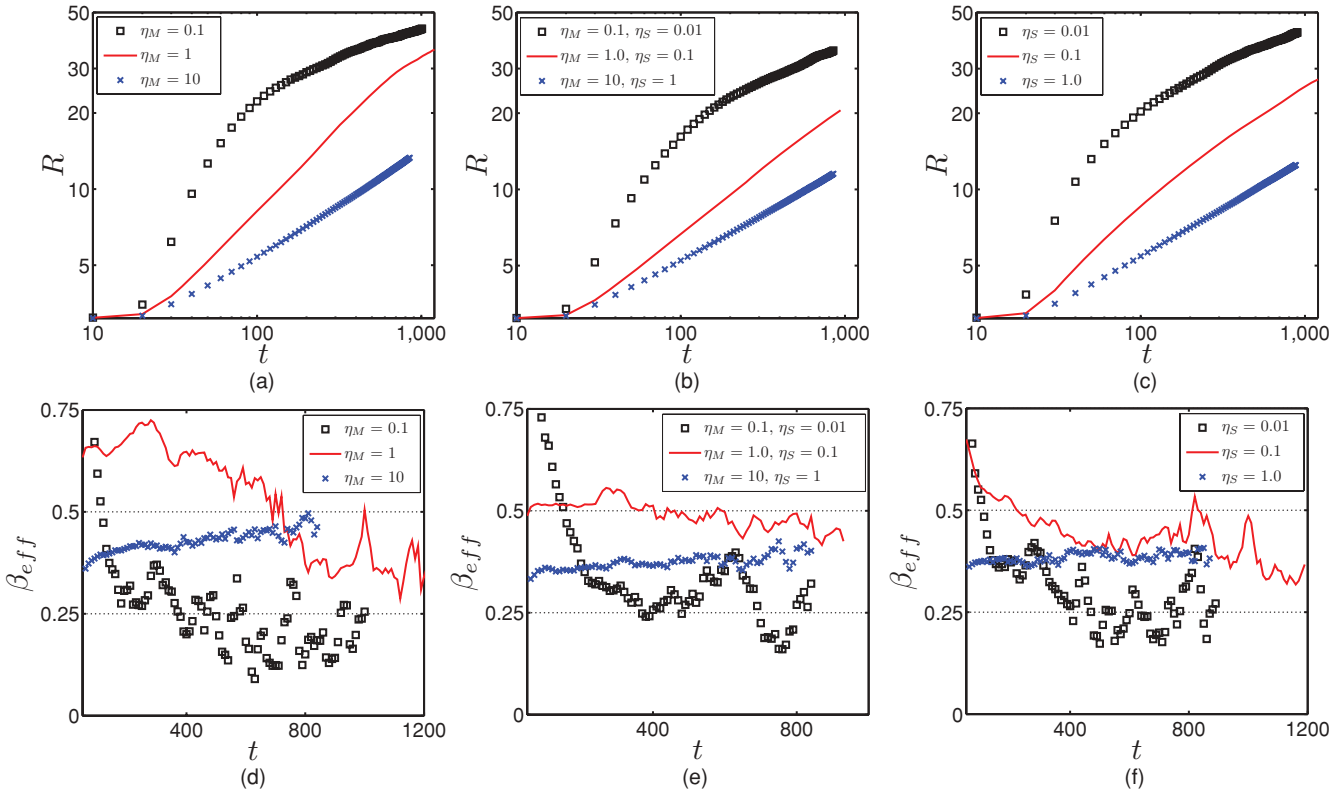

FIG. 5. Comparison of R vs t [(a)–(c)] and β_{eff} vs t [(d)–(f)] for different ℓ_H. From left to right, $\ell_H = \infty$, 10, and 0, respectively. In all cases, decreasing the viscosities implies faster domain growth. Note the emergence of an apparent scaling regime for $\ell_H = 10$ at intermediate viscosity values with $\beta_{\text{eff}} \approx 0.5$, shown in panel (e), solid line.

apart from the high-viscosity case which displays behavior consistent with standard Ostwald ripening. Not surprisingly, increasing the viscosity leads to the standard Ostwald ripening scaling regime $\beta_{\text{eff}} \approx 1/3$ regardless of the value of ℓ_H over the range of simulation times explored in this study.

In order to quantitatively analyze the breakdown of dynamical scaling, we have investigated the coarsening behavior of domains with different morphologies, ranging from elongated to more isotropic. To this end, we first identified all domains in the system, defined as a set of connected, nearest neighbor lattice sites. Then, a dimensionless geometric quantity, denoted by γ, was computed for each domain. Here, $\gamma \equiv \pi A^{-2} \int \mathbf{r}^2 dA$, with A denoting the area of the domain; the integration is with respect to the center of mass of the domain. Based on the value of γ, every domain is categorized either as elongated ($\gamma > 3/4$) or circular ($\gamma \leq 3/4$). For comparison, $\gamma = 1/2,\ 5/8,$ or $5/6$ for a perfect circle, ellipse with $a = 2b$, or ellipse with $a = 3b$, respectively. We have verfied that the results of the quantitative analysis presented below are not sensitive to the specific choice of the threshold value for $\gamma < 1$.

Next, we extracted the average domain sizes R^{elong} and R^{circ} by employing the definitions $R^{\text{elong}}(t) = \sum_{i=1}^{n} A_i^{\text{elong}} / \sum_{i=1}^{n} \ell_i^{\text{elong}}$ and $R^{\text{circ}}(t) = \sum_{j=1}^{m} A_j^{\text{circ}} / \sum_{j=1}^{m} \ell_j^{\text{circ}}$, where A_i^{elong} (A_j^{circ}), and ℓ_i^{elong} (ℓ_j^{circ}) denote the area and interface length of the ith elongated (jth circular) domain at time t, and the summations run over all elongated and circular domains, respectively. The effective growth exponents $\beta_{\text{eff}}^{\text{elong}}$ and $\beta_{\text{eff}}^{\text{circ}}$ corresponding to the different domain shapes in turn were obtained from R^{elong} and R^{circ} using the same procedure as in the case of β_{eff}. The data is displayed in Figs. 6–8. In the effectively 2D case ($\ell_H = \infty$; Fig. 6), at intermediate values of membrane viscosity corresponding to $Pe \sim 1$ ($\eta_M = 1$ in Fig. 6(b)), elongated domains coarsen rapidly with $\beta_{\text{eff}}^{\text{elong}} \approx 0.7$ initially and $\beta_{\text{eff}}^{\text{elong}} \approx 0.5$ at the end of the simulation, while circular ones coarsen more slowly with $\beta_{\text{eff}}^{\text{circ}}$ which also decreases in time. The high initial values of $\beta_{\text{eff}}^{\text{circ}}$ result from coalescence events facilitated by the flow field. For $\eta_M = 0.1$ corresponding to $Pe \sim 10$, on the other hand, both $\beta_{\text{eff}}^{\text{elong}}$ and $\beta_{\text{eff}}^{\text{circ}}$ quickly decrease towards $\approx$0.25, as shown in Fig. 6(d).

In the $\ell_H = 10$ case (Fig. 7), on the other hand, at intermediate values of $\eta_M = 1$ and $\eta_S = 0.1$, corresponding to $Pe \sim 1$ shown in Fig. 7(b), $\beta_{\text{eff}}^{\text{elong}} \approx 0.5$ for the duration of the simulation, while $\beta_{\text{eff}}^{\text{circ}}$ decreases towards $1/3$. Notably, the overall $R(t)$ follows very closely that corresponding to the elongated shapes. This implies that the number of circular domains relative to the elongated ones is small, consistent with visual observations of configurations displayed in Fig. 3. The scaling we observe is only apparent, however, as domains with different shapes coarsen with different rates. As the viscosities are decreased to $\eta_M = 0.1$ and $\eta_S = 0.01$ corresponding to $Pe \sim 10$, we find no apparent scaling regime, as both $\beta_{\text{eff}}^{\text{elong}}$ and $\beta_{\text{eff}}^{\text{circ}}$ quickly decrease towards 0.3 (see Fig. 7(d)). In this case, the overall $R(t)$ deviates significantly

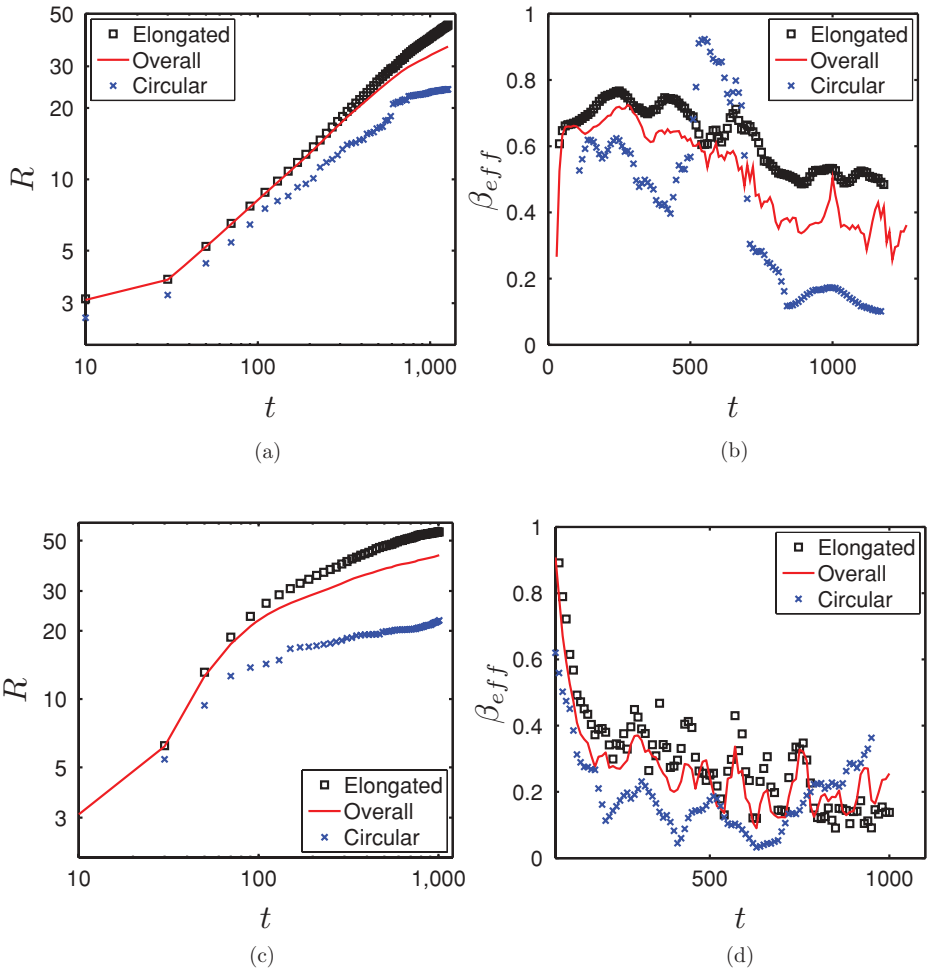

FIG. 6. Comparison of domain growth kinetics for elongated vs circular domains for $\ell_H = \infty$. (a), (c) $R(t)$. (b), (d) $\beta_{\text{eff}}(t)$. Top panels: $\eta_M = 1$. Bottom panels: $\eta_M = 0.1$. In both cases, the average elongated domain size is larger than the average circular domain size. We note that the discontinuities in the $\beta_{\text{eff}}^{\text{circ}}$ vs t data for the circular domains result from circular domain coalescence events as well as from elongated domains becoming circular ones within our categorization scheme. Notice the absence of any scaling regimes.

from that corresponding to the elongated shapes. This implies that the number of circular domains relative to the elongated ones is large, again consistent with visual observations of configurations displayed in Fig. 3.

Finally, in the $\ell_H = 0$ case (Fig. 8), at an intermediate value of $\eta_S = 0.1$ corresponding to $Pe \sim 10$, shown in Fig. 8(b), $\beta_{\text{eff}}^{\text{elong}} \approx 0.6$ initially and $\beta_{\text{eff}}^{\text{elong}} \approx 0.4$ at the end of the simulation, while the circular ones coarsen more slowly with $\beta_{\text{eff}}^{\text{circ}}$ which decreases in time towards 0.3. Furthermore, the overall $R(t)$ follows very closely that corresponding to the elongated shapes. As in the previous two cases, at lower values of η_S corresponding to $Pe \sim 100$ we find no apparent scaling regime; instead $\beta_{\text{eff}}^{\text{elong}}$ and $\beta_{\text{eff}}^{\text{circ}}$ quickly decrease towards 0.2, as shown in Fig. 8(d).

To summarize, regardless of the specific value of ℓ_H, at high viscosities corresponding to $Pe \ll 1$, both elongated and circular domains coarsen with $\beta_{\text{eff}}^{\text{elong}} = \beta_{\text{eff}}^{\text{circ}} \approx 0.3$, in accordance with diffusion-mediated Ostwald ripening. On the other hand, for intermediate viscosity values corresponding to $Pe \lesssim 10$, elongated domains initially coarsen with an effective exponent $\beta_{\text{eff}}^{\text{elong}} \sim 0.6$ which smoothly decreases in time, while $\beta_{\text{eff}}^{\text{circ}} \approx 0.3$. Finally, at lower viscosities corresponding to $Pe \gtrsim 10$, both $\beta_{\text{eff}}^{\text{elong}}$ and $\beta_{\text{eff}}^{\text{circ}}$ rapidly decrease towards 0.3.

IV. DISCUSSION AND CONCLUDING REMARKS

In this paper, we have studied hydrodynamic flow effects on spinodal decomposition kinetics in lipid bilayer membranes. Our simulation results conclusively demonstrate the breakdown of dynamical scaling in the SD kinetics during phase separation in lipid bilayers in the viscously dominated flow regime at high Peclét numbers, where convective transport dominates over diffusive one. It is precisely this $Pe \gg 1$ regime which is relevant for lipid microdomains on the scale of $\sim 10^{-6}$ m or greater. Indeed, following the arguments in Ref. 17, we estimate that the *effective* Peclét number Pe^*, obtained from Pe by replacing the correlation length ξ with the characteristic domain size R, is given by $\sim \Gamma R/(4\pi k_B T)$, where $\Gamma \sim 1$ pN denotes the line tension of a lipid microdomain boundary.[4] For a typical domain size $R \sim 10^{-5}$ m, we obtain $Pe^* \sim 10^3$ at room temperature. Thus, the breakdown of dynamical scaling due to hydrodynamic effects

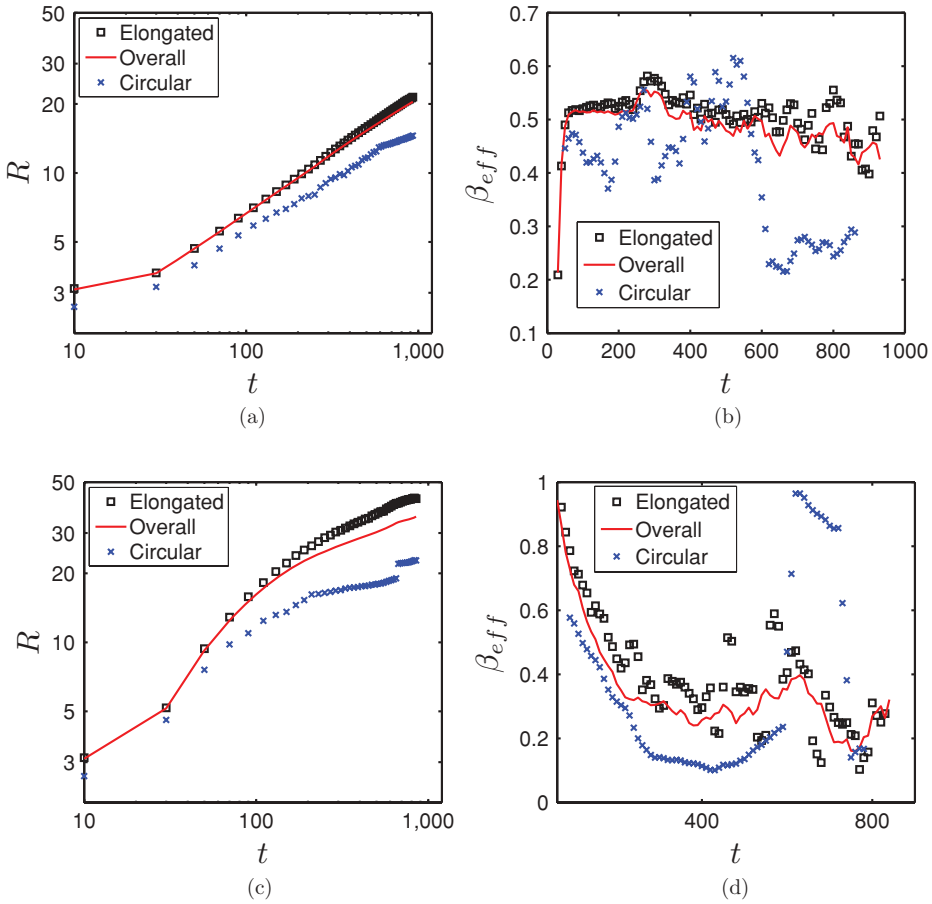

FIG. 7. Comparison of domain growth kinetics for elongated vs circular domains for $\ell_H = 10$. (a), (c) $R(t)$. (b), (d) $\beta_{\text{eff}}(t)$. Top panels: $\eta_S = 0.1$. Bottom panels: $\eta_S = 0.01$. Notice the presence of an apparent scaling regime over the attainable simulation time window with $\beta_{\text{eff}} \approx \beta_{\text{eff}}^{\text{elong}} \approx 0.5$ at intermediate viscosity values corresponding to $Pe \sim 1$, shown in panel (b), solid line. In this particular case, circular domains contribute very little to the overall average domain size.

should be readily observable in experiments employing model membrane systems. The breakdown of dynamical scaling reported here has been previously observed in strictly 2D simulations of phase-separating binary fluids.[15,16,30] In the case of lipid bilayers embedded within a 3D solvent, we demonstrated that the growth mechanisms and effective exponents are different for elongated versus circular domains, leading to the absence of dynamical scaling. With regard to circular domains, they are simply passively advected by the membrane flow field and initially coarsen via coalescence events, while elongated domains coarsen rapidly as driven by flow fields generated by large curvature variations along compositional interfaces. Furthermore, the values of the effective coarsening exponents depend on both membrane and solvent viscosities. Interestingly, for some viscosity values corresponding to $Pe \sim 1$, an *apparent* scaling regime was found in the presence of solvent, for which the effective coarsening exponent $\beta_{\text{eff}} \approx 0.5$. Such effective coarsening exponents have also been reported by Kumar *et al.*[12] in a DPD simulation study and by Camley and Brown,[14] who employed a similar continuum model to the one presented here.

As in the recent DPD simulation study of phase separation in thin liquid films by Ramachandran *et al.*,[13] we find that the absence of the solvent quantitatively alters the SD kinetics. More specifically, upon removing the solvent, the coarsening rate increases relative to the fully 3D case at fixed membrane viscosity, and this is reflected in larger effective coarsening exponents. The values of the effective coarsening exponents we observe, however, are significantly larger than those reported in Ref. 13. This difference can be attributed to the dominance of the Brownian coagulation mechanism of the domains observed in the DPD simulations versus the large-scale shape changes corresponding to the elongated domains found in our simulations. However, we expect that large-scale DPD simulations (or other particle-based methods, for that matter) should be able to probe the processes leading to the breakdown of dynamical scaling at the critical composition, especially in the $Re \ll 1$ and $Pe \gg 1$ limit.

With regard to off-critical compositions, additional simulations we have carried out indicate that circular domains initially coarsen rapidly in the case of intermediate values of the viscosity and for all values of ℓ_H investigated. More specifically, $\beta_{\text{eff}}^{\text{circ}} \approx 0.6$ initially and $\beta_{\text{eff}}^{\text{circ}} \approx 0.3$ at later times, with the decay rate of $\beta_{\text{eff}}^{\text{circ}}$ in time determined by the magnitude of the viscosity. Thus, depending on the observation window and viscosities, a broad range of effective exponents can be extracted. These observations may in part explain the variance in the experimentally extracted exponents reported in the literature.[8,9] Once a droplet morphology is attained after

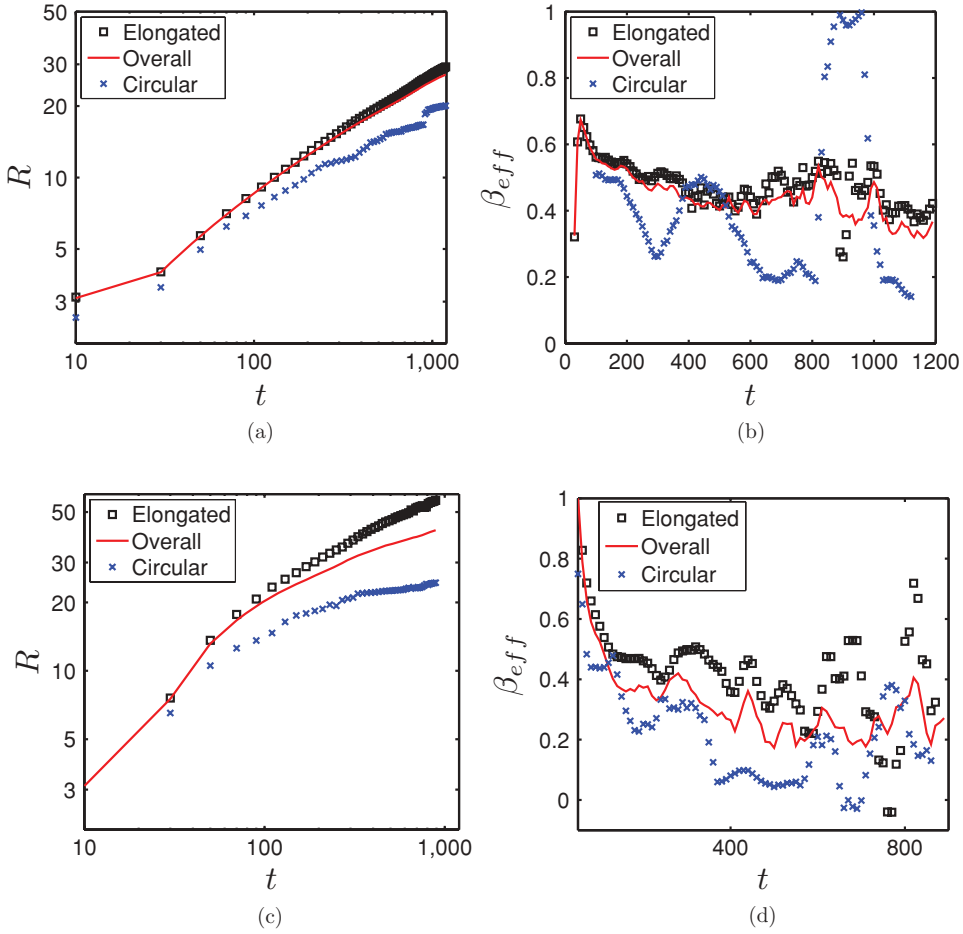

FIG. 8. Comparison of domain growth kinetics for elongated vs circular domains for $\ell_H = 0$. (a), (c) $R(t)$. (b), (d) $\beta_{\text{eff}}(t)$. Top panels: $\eta_S = 0.1$. Bottom panels: $\eta_S = 0.01$. Notice the absence of any scaling regimes.

these transients, however, advective transport contributes very little as far as domain growth is concerned. In the absence of thermal fluctuations, the domains asymptotically coarsen with $R(t) \sim t^{1/3}$ due to Ostwald ripening, regardless of the value of ℓ_H. The presence of thermal fluctuations, on the other hand, in addition to making the compositional interfaces more diffuse, introduces a distinct coarsening mechanism. In particular,droplets of the minority phase diffuse around due to thermal fluctuations and coalesce upon impingement; that is, the Brownian coagulation mechanism eventually dominates. As discussed in Ref. 13, this process leads to $R(t) \sim t^{1/2}$ when $R \ll \ell_H$, and $R(t) \sim t^{1/3}$ when $R \gg \ell_H$. In contrast to systems at critical composition, we expect that dynamic scaling in off-critical systems is established asymptotically regardless of the value of ℓ_H.

In summary, we have demonstrated that the presence of membrane and solvent hydrodynamic flow fields dramatically affects spinodal decomposition kinetics in lipid bilayer membranes at the critical composition. In particular, we have unequivocally shown that dynamical scaling is absent in such systems in the viscously dominated flow regime at large Peclét numbers. Currently, we are investigating the roles of composition-dependent viscosity and fluid inertia on coarsening kinetics in lipid bilayer membranes, and hope to report on this in the near future.

ACKNOWLEDGEMENTS

This work has been in part supported by NSF-DMR Grants Nos. DMR-0449184 and DMR-1006831.

[1] L. A. Bagatolli and E. Gratton, J. Fluoresc. **11**, 141 (2001).
[2] S. L. Veatch and S. L. Keller, Phys. Rev. Lett. **89**, 268101 (2002).
[3] P. Cicuta, S. L. Keller, and S. L. Veatch, J. Phys. Chem. B **111**, 3328 (2007).
[4] S. L. Veatch, P. Cicuta, P. Sengupta, A. R. Honerkamp-Smith, D. Holowka, and B. Baird, Chem. Biol. **3**, 287 (2008).
[5] A. R. Honerkamp-Smith, S. L. Keller, and S. L. Veatch, Biochem. Biophys. Acta **1788**, 53 (2009).
[6] M. Haataja, Phys. Rev. E. **80**, 020902 (2009).
[7] A. J. Bray, Adv. Phys. **51**, 481 (2002).
[8] D. Saeki, T. Hamada, and K. Yoshikawa, J. Phys. Soc. Jpn. **75**, 013602 (2006).
[9] M. Yanagisawa, M. Imai, T. Masui, S. Komura, and T. Ohta, Biophys. J. **92**, 115 (2007).
[10] M. Laradji and P. B. S. Kumar, Phys. Rev. Lett. **93**, 198105 (2004).
[11] M. Laradji and P. B. S. Kumar, Phys. Rev. E **73**, 040901 (2006).
[12] S. Ramachandran, M. Laradji, and P. B. S. Kumar, J. Phys. Soc. Jpn. **78**, 041006 (2009).
[13] S. Ramachandran, S. Komura, and G. Gompper, EPL **89**, 56001 (2010).
[14] B. A. Camley and F. L. H. Brown, Phys. Rev. Lett. **105**, 148102 (2010).
[15] H. Tanaka and T. Araki, Phys. Rev. Lett. **81**, 389 (1998).
[16] A. J. Wagner and J. M. Yeomans, Phys. Rev. Lett. **80**, 1429 (1998).
[17] N. Vladimirova, A. Malagoli, and R. Mauri, Phys. Rev. E **60**, 6968 (1999).
[18] P. C. Hohenberg and B. I. Halperin, Rev. Mod. Phys. **49**, 435 (1977).

[19]Experimentally, it has been verified that the no-slip boundary condition holds down to the nanometer length scales in supported monolayers and bilayers; see, e.g., B. Cross, A. Steinberger, C. Cottin-Bizonne, J.-P. Rieu, and E. Charlaix, Europhys. Lett. **73**, 390 (2006). In cases where slip cannot be ignored, Eq. (6) can be modified accordingly to incorporate a finite slip length ℓ_s via $\hat{T}_{\alpha\beta}(\mathbf{q}) = [1/\eta_M q^2 + 2\eta_S q/(1+q\ell_s)]\left[\delta_{\alpha\beta} - (q_\alpha q_\beta)/q^2\right]$.
[20]K. Inaura and Y. Fujitani, J. Phys. Soc. Japan **77**, 114603 (2008).
[21]P. G. Saffman and M. Delbrück, Proc. Nat. Acad. Sci. U.S.A. **72**, 3111 (1975).
[22]E. D. Siggia, Phys. Rev. A **20**, 595 (1979).
[23]H. Furukawa, Phys. Rev. A **30**, 1052 (1984).
[24]M. S. Miguel, M. Grant, and J. D. Gunton, Phys. Rev. A **31**, 1001 (1985).
[25]P. Ossadnik, M. F.Gyure, H. E. Stanley, and S. C. Glotzer, Phys. Rev. Lett. **72**, 2498 (1994).
[26]G. Leptoukh, B. Strickland, and C. Roland, Phys. Rev. Lett. **74**, 3636 (1995).
[27]E. Velasco and S. Toxvaerd, Phys. Rev. E **54**, 605 (1996).
[28]T. Lookman, Y. Wu, F. J. Alexander, and S. Chen, Phys. Rev. E **53**, 5513 (1996).
[29]P. V. Coveney and K. E. Novik, Phys. Rev. E **54**, 5134 (1996).
[30]H. Furukawa, Phys. Rev. E **61**, 1423 (2000).
[31]J. Chin and P. V. Coveney, Phys. Rev. E **66**, 016303 (2002).
[32]A. Shinozaki and Y. Oono, Phys. Rev. E **48**, 2622 (1993).
[33]T. Han, J. Fan, and M. Haataja (unpublished).